MODELLISTICA E CALCOLO SCIENTIFICO

MOX

MODELING AND SCIENTIFIC COMPUTING

MOX-Report No. 61/2017

Three-dimensional fault representation by interface and solid elements: effects of the anisotropy of the fault zone permeability on the timing of triggered earthquakes

Vadacca, L.; Colciago, C. M.; Micheletti, S.; Scotti, A.

Three-dimensional fault representation by interface and solid elements

Effects of the anisotropy of the fault zone permeability on the timing of triggered earthquakes

Luigi Vadacca · Claudia Maria Colciago · Stefano Micheletti · Anna Scotti

Abstract In the last years numerous seismological evidences have shown a strict correlation between fluid injection and seismicity. An important topic that is currently under discussion in the scientific community concerns the prediction of the earthquake magnitude that may be triggered by fluid injection activities. Coupled fluid flow and geomechanical deformation models can aim at understand the evolution of pore pressure and rock deformation due to fluid injection in the subsurface. To perform an accurate numerical study of the correlation among fluid injection, seismicity rates and maximum earthquake magnitude, it is necessary to characterize the model with two fundamental features: first, the presence of a system of faults possibly intersecting among each other; second, the variability of the hydro-mechanical properties across the region surrounding each fault plane (fault zone). The novelty of this work is to account for these two aspects combining together two different numerical techniques that have been proposed in literature for the fault's modelling: for the first feature, *interface elements* are used to describe the frictional contacts occurring on the faults surfaces; for the second feature, *solid elements* are adopted to describe the heterogeneous hydro-mechanical behavior across the fault zone. Moreover, we account for a spatial variation of the permeability in the fault zone both along the dip and the normal direction with respect to the fault plane. We compute the numerical solution for six models among which we vary the permeability contrasts between protolith rocks and damage zone and between damage zone and fault core. We demonstrate that the anisotropy of permeability of the fault zone has a strong impact both on the timing and on the magnitude of triggered earthquakes. We suggest that a similar approach, which includes the entire architecture of the fault zone, shall be included in fluid-flow-geomechanical simulations to improve fault stability analysis during fluid injection.

Keywords Fault zone permeability · Fault reactivation · Geomechanics modelling · Triggered earthquakes · Fluid injection

Luigi Vadacca
MOX, Department of Mathematics, Politecnico di Milano
Piazza L. da Vinci 32, Milano, 20133, Italy
Tel.: +39-02-23994633
E-mail: luigi.vadacca@polimi.it

Claudia Maria Colciago
CMCS–MATHICSE–SB, École Polytechnique Fédérale de Lausanne
Av. Picard, Station 8, Lausanne, CH–1015, Switzerland

Stefano Micheletti · Anna Scotti
MOX, Department of Mathematics, Politecnico di Milano
Piazza L. da Vinci 32, Milano, 20133, Italy

1 Introduction

The possibility of fault reactivation during fluid injection activities represents one of the most important aspects that have to be accurately estimated to reduce the risk of leakage and hence to maintain the integrity of a storage aquifer. Indeed, faults can represent excellent impermeable barriers that constrain the fluids to remain inside the reservoir or storage aquifer. However, if the critical frictional strength is overcome, faults reactivate triggering slips (e.g. earthquake). During this phase the fault permeability could suddenly increase and hence, faults could become preferential pathways for the migration of fluids away from the reservoir [7, 48,45]. Recent works have demonstrated a strict correlation between the increase of microseismicity rates and fluid injection [46]. Only few evidences of moderate earthquakes have been linked to fluid injection, in

particular by injection of wastewater where large volumes of fluids are involved [24,32]. Understanding the fault mechanics and the architecture of the fault zone became hence a fundamental issue to be considered during fluid injection activities. Slip tendency, maximum expected slip magnitude and Coulomb stress change analysis have been used to understand the behavior of natural earthquakes and hence can be applied also to the study of induced and triggered earthquakes [30,10, 44,28,40]. However only coupled fluid flow and geomechanical deformation models can aim at successfully understand the evolution of pore pressure and rock deformation due to fluid injection in the subsurface. For this reason an accurate numerical model for the faults is fundamental [33,9,8,23]. Two main approaches have been proposed in the literature to model the fault deformation: explicit representation of the fault plane with interface elements (e.g. [1] and references therein) and equivalent continuum representation of the fault zone with solid elements [9,8]. The first one has the advantage to constrain the slip along a surface through realistic friction constitutive law (e.g. rate-and state-friction [14]), the second one is better suited for the simulation of the evolution of the deformation across the fault zone during the interseismic and postseismic phases of the seismic cycle. However, in the equivalent continuum method, the displacement is computed as a continuum function, yielding a poor approximation of the slip itself and, thus, also a poor approximation of the magnitude of triggered earthquake compared to the one obtained with the explicit representation. These approaches generally do not take into account changes in the hydromechanical properties within the fault zone. In fact, two main hydromechanical layers characterize a fault zone: the fault core and the damage zone. The fault core is composed mainly of breccia and gouge, and is characterized by fine-grain material that is continuously crumbled during several earthquakes. This layer represents the part of the fault zone with the lowest permeability. Most of the coseismic slip occurs along rupture surfaces inside the fault core [38]. The damage fault zone is a wider layer that surrounds the fault core and features lenses of breccia and a network of macroscopic fractures. This is the most permeable layer of the fault zone. Experimental results show that the permeability of the damage zone can be one to three orders of magnitude greater than the permeability of protolith and four to six orders of magnitude greater than the permeability of the core, both in dip and in normal direction with respect to the fault plane [41,31,5,7,47,43, 29,27]. The variability strictly depends on the lithology and its level of chemical and physical alteration [7].

In this work we perform three-dimensional coupled fluid flow and geomechanical deformation simulations of fault reactivation by water injection. We aim at studying the behavior of the reservoir system in simultaneous presence of two factors: the frictional contacts of the faults, modelled by interface elements, and the spacial variability of the permeability in the fault zones. At the best of our knowledge, no pre-existing published work focused on the effects of these two important factors. Moreover, we let the fault zone permeability variates both in the dip and in the normal direction with respect to the fault plane and we consider different permeability contrast between protolith rocks and damage zone and between damage zone and caprock. We demonstrate that the anisotropy of the fault zone permeability has a strong impact both on the timing and on the magnitude of triggered earthquakes.

2 Hydro-mechanical modelling of faulted storage aquifers

2.1 Governing equations in porous media

Assuming small deformations and isothermal conditions, the governing equations for coupled flow and geomechanics are derived from conservation of mass and balance of linear momentum. The quasi-static governing equations for linear momentum balance of the solid/fluid system on a 3D spatial domain Ω can be expressed as

$$\nabla \cdot \boldsymbol{\sigma} + \rho_b \boldsymbol{g} = \boldsymbol{0} \quad \text{in } \Omega \tag{1}$$

with $\boldsymbol{\Omega}$ the Cauchy total stress tensor, $\boldsymbol{g}$ the gravity acceleration vector, $\phi_b = \phi \rho_f + (1-\phi)\rho_s$ the bulk density, ρ_f the total fluid density, ρ_s the solid-phase density and ϕ the porosity that is the ratio of voids to the total volume. In this work we consider an isothermal single-phase flow of a fluid (water) with no stress dependence of permeability in the bulk, so that the single fluid mass conservation equation reduces to

$$\frac{dm}{dt} + \nabla \cdot \boldsymbol{w} = \rho_f f \tag{2}$$

where m is the fluid mass, f is the volumetric source, $\boldsymbol{w} = \rho_f \boldsymbol{v}$ is the fluid mass flux and $\boldsymbol{v}$ is the fluid velocity given by Darcy law:

$$\boldsymbol{v} = -\frac{\boldsymbol{k}}{\mu_f}(\nabla p_f - \rho_f \boldsymbol{g}) \tag{3}$$

where $\boldsymbol{k}$ is the permeability, μ_f is the fluid dynamic viscosity and p_f is the pore fluid pressure [3]. Variations of pore fluid pressure affect the effective stress.

We assume that the porous medium is fully saturated with water. In this way the relationship between effective stress ($\boldsymbol{\sigma}'$), total stress ($\boldsymbol{\sigma}$) and pore pressure (p_f) reduces to the Terzaghi effective stress principle:

$$\boldsymbol{\sigma}' = \boldsymbol{\sigma} + p_f \qquad (4)$$

Then the deformation of the porous medium affects the fluid mass in the voids and hence, the porosity itself and the pore pressure.

2.2 Fault zone representation by coupled interface-solid elements

In order to model the deformation along the fault plane, we use an explicit representation of the fault with interface elements (see Figure 2 for a schematic representation in two dimensional domain where, thus, the faults are represented by one dimensional lines and the elements are indeed one-dimensional segments). The nodes of the mesh along the fault surfaces are duplicated, new node-IDs are assigned to the new nodes, and the mesh connectivity is updated. In this way, each fault is characterized by two surfaces (lines in 2D) that are geometrically coincident but distinct from the numerical point of view: one surface belongs to the hanging-wall block and the second one to the footwall block (Figure 2). This split node procedure allows us to compute a different displacement for the two surfaces: we denote $\boldsymbol{u}_+$ the displacement of the nodes lying on the hanging wall surface and $\boldsymbol{u}_-$ the one of footwall surface nodes. The definition of the slip $\boldsymbol{d}$ on the fault surface is then straightforward:

$$\boldsymbol{d} = \boldsymbol{u}_+ - \boldsymbol{u}_-. \qquad (5)$$

We are interested in modeling buried faults and, moreover, we assume that no crack propagation phenomena are occurring; thus, in order to avoid numerical instabilities we duplicate only the nodes that are strictly *internal* to the surface, thus keeping unique the ones lying on the fault boundary perimeter. This procedure is not necessary in case the fault's perimeter lies on the boundaries of the entire domain itself.

Furthermore, we aim at enriching our model with an additional features that augment its complexity: in fact, we are interested in modelling also intersecting faults and, in particular, T-shape intesections. These faults are treated as non-intersecting faults and the nodes along the tip line of the first fault are merged with the one along the hanging-wall or footwall surface of the second fault (depending on the location of
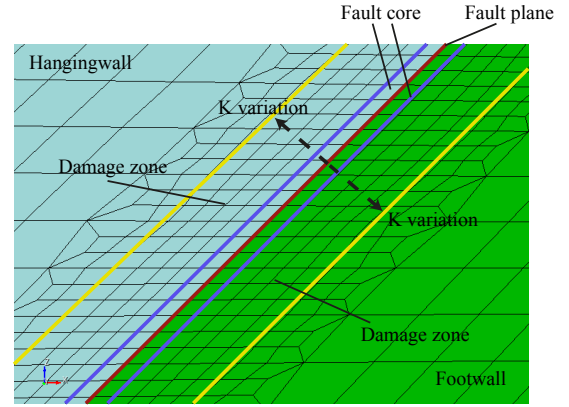
Fig. 1: View of the fault zone representation considered in this work.

(a) Single fault

(b) T-shape intersection
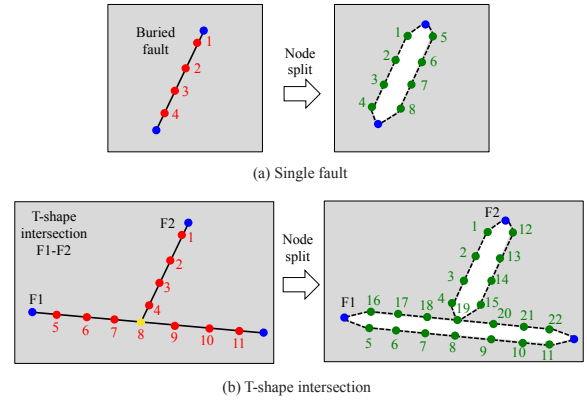
Fig. 2: Two dimensional representation of the node split for a single fault (a) and for a T-shape intersection (b). Each one of the red nodes is split into two geometrically coincident nodes, while the fault's boundary blue nodes are kept as unique nodes. The yellow node in (b), as an internal node of the fault F1, is also split into two green nodes. The white space between the green nodes is not a pysical space but rather an artificial space added for the sake of an easier graphical representation.

the second fault, Figure 2b). The fault reactivation is modeled by the Amontons law:

$$\tau = \mu \sigma'_n \qquad (6)$$

where $\sigma'_n = (\boldsymbol{\sigma}\boldsymbol{n}) \cdot \boldsymbol{n}$ is the effective normal traction ($\boldsymbol{n}$ is the normal vector to the fault surface, $\sigma'_n = \sigma_n - p_f$; σ_n is positive in compression), $\tau = \boldsymbol{\sigma}\boldsymbol{n} - \sigma_n\boldsymbol{n}$ is the shear stress modulus, and μ is the sliding friction (e.g. $\mu = 0.6 - 0.8$ [6]; $\mu \leq 0.4$ depending on the presence of clay mineral [35,4,13,26]). From (6), we calculate the

slip tendency (ST) factor as the ratio of shear stress to normal stress acting on the plane of weakness [39]:

$$ST = \tau/\sigma'_n. \tag{7}$$

The slip tendency indicates if one fault is in a stable or unstable state of stress: if $ST < \mu$ the the state of stress is stable and no slip occurs along the fault plane. Otherwise, if $ST \geq \mu$ the strength of the fault is overcome and slip starts to propagate along the fault plane. We use a static friction constitutive model to describe the evolution of the slip after the rupture. In this model μ is constant, meaning that once the fault strength is overcome, the fault slips at a steady rate. In order to model the spatial variation of the fault zone permeability, a local mesh refinement is performed around the fault surfaces along the normal direction. The damage zone and the fault core are discretized in one elements and four elements layers, respectively (Figure 1). Appropriate hydro-mechanical properties are associated to these elements (see section 2.4).

2.3 Coupled fluid-solid-faults system of equations

We aim at writing the coupled system of equations together with the contact constrain that is needed to be solved to model a reservoir in presence of faults. Let us denote Ω the entire domain and $\Gamma = \cup_i \Gamma_i$ the union of the surfaces Γ_i composing the fault system. After some manipulation of (1), (2), the system of equations can be written as follows:

$$\begin{cases} \nabla \cdot (\boldsymbol{\sigma}'(\boldsymbol{u}) - p_f) + \rho_b \boldsymbol{g} = \boldsymbol{0} & \text{in } \Omega \\ \dfrac{1}{M}\dfrac{\partial p_f}{\partial t} + \dfrac{\partial \varepsilon_v(\boldsymbol{u})}{\partial t} - \rho_f \nabla \cdot \left(\dfrac{\boldsymbol{k}}{\mu_f}\nabla p_f - \rho_f \boldsymbol{g}\right) = \rho_f f & \text{in } \Omega \\ \boldsymbol{d} = \boldsymbol{0} \quad \text{if } ST < \mu & \text{on } \Gamma \\ \boldsymbol{u}_+ - \boldsymbol{u}_- - \boldsymbol{d} = \boldsymbol{0} \quad \text{if } ST \geq \mu & \text{on } \Gamma \end{cases} \tag{8}$$

where M is the Biot modulus that depends on the fluid compressibility and the bulk modulus of the solid grain,

$$\boldsymbol{\sigma}'(\boldsymbol{u}) = C_{dr} : \boldsymbol{\varepsilon} \quad \text{and} \quad \varepsilon_v(\boldsymbol{u}) = tr(\boldsymbol{\varepsilon}), \tag{9}$$

with

$$\boldsymbol{\varepsilon} := \frac{1}{2}(\nabla \boldsymbol{u} + \nabla^T \boldsymbol{u}) \tag{10}$$

and C_{dr} is the tensor of the coefficients that define the constitutive stress strain relation of the poroelastic material. The unknowns of system (8) are indeed the displacement $\boldsymbol{u}$, the slip field $\boldsymbol{d}$, and the pore fluid pressure

p_f. The effective and total stress fields σ and σ', as well as the deformations ε and the slip tendency ST depend on the values of the unknown fields and can be calculated once the system variables are computed. The other symbols apprearing in (8), i.e. ρ_f, ρ_s, ρ_b, f, $\boldsymbol{g}$, $\boldsymbol{k}$, μ_f, C_{dr}, M, μ, are parameters and/or input data and their values will be specified in section 2.4.

System (8) is then endowed by boundary conditions on $\partial\Omega$. Moreover, an equilibrium solution for $\boldsymbol{u}$ and p_f is computed and used as temporal initial condition. More details about boundary and initial conditions are described in section 2.4.

We refer to the work of [23] for a complete mathematical description of poroelasticity for single and multiphase fluid system and for the details about the derivation of the equations of system (8). There are two common approaches to solve the coupled balance equations (8),(1) and (2). One is the sequential solution method that consists in solving first the stress balance equation and, second, using these results to solve the mass balance equation. The results of the second step are then plugged in the stress balance equation to compute again the displacement and the stress state of the system (e.g. [34,25,23]). The second approach consists in solving the coupled system directly. This approach is used by the commercial software package ABAQUS/Standard ([2]) that is used in this work to perform the coupled pore pressure and stress analysis of faulted storage aquifers.

2.4 Model setups

The geometry consists of a block of $25 \times 25 \times 6$ km with different horizontal layers representing the permeable storage aquifer, the low-permeable cap rocks and the upper and basal aquifers (Figure 3a-b). The storage aquifer, the cap rocks and part of the upper aquifer are cut by a fault system that is characterized by four $45°$ dipping faults and two vertical faults. The vertical faults are located in the central part of the block and forming a T-shaped intersection with two of the $45°$ dipping faults (Figure 3c).These faults, together with the cap rocks, define the limits of the volume of storage aquifer where water injection is simulated. Two other smaller faults are present inside the storage aquifer (Figure 3b-c). They are cutting the same horizontal multilayer domain without intersecting the vertical faults.

The simulation consists in two different steps. In the first one we apply a gravitational loading and an initial stress field on the entire model (geostatic step). We define a compressive stress regime where the maximum (SH) and middle (Sh) stress axis are horizontal

and parallel to the x-and y-axis; respectively. The minimum stress axis is vertical (Sv). The ratios between SH and Sv is 2.2 and the one between Sh and Sv is 1.5. These are chosen in order to obtain an initial value of slip tendency near to the critical one along the 45° dipping faults (a critical slip tendency of 0.4 is assumed). In this step the model sides and bottom are fixed in normal direction, whereas the top of the model is free to move in all directions. We consider a hydrostatic initial pore pressure on the nodes of the entire model and this pore pressure is maintained hydrostatic value along the boundaries at all times. In this way no variation of pore pressure can occur along the boundaries.

After this first step, the system is at equilibrium and the solution is used as the initial condition for the second step. Fluid injection is simulated ([2]) by applied at one node at a depth of 2250 m into the storage aquifer (Figure 3c). The pressurized zone is located at a distance of about 1 km from the reservoir-bounding fault F1 and from the fault F2 located in the inner part of the reservoir (Figure 3b-c). The total volume of water injected is equal to 98 m^3 over 24 steps following the cubic function represented in Figure 4. The boundary conditions are the same as the one for the geostatic step. The hydro-mechanical properties for the faulted storage aquifer-caprock system are described in table 1, 2 and table 3. The properties that define each layer are always the same for all the different settings considered in this work. Only the permeability across the damage zone and the fault core varies depending on the distance from the fault surface (Figure 1).

Depending on different permeability contrasts between protolith and damage zone (k_d/k_p) and between damage zone and fault core (k_d/k_c), six model sets are studied (Table 2 and 3). In Model$_1$ the permeability of the damage zone is one order of magnitude higher than the permeability of the protolith ($k_d/k_p = 10^1$). Note that this contrast is always maintained constant depending on the type of protolith that the damage zone intersects. Concerning the fault core, its permeability is maintained constant at a value of 10^{-22} m^2, hence the contrast between damage zone and fault core is variable in space across layers (Table 2, 3). As in the Model$_1$, also in Model$_2$ the permeability of the damage zone is one order of magnitude higher than the permeability of the protolith ($k_d/k_p = 10^1$, Table 1, 2, and 3). The only difference is that, in this model, the permeability of the fault core is maintained constant at a value of 10^{-16} m^2 (Table 2, 3). In Model$_1$ and Model$_2$ we consider only the end-member values of fault core permeability found in literature ([17,7,29]). On the contrary in the other models we assume a direct correlation between the fault core permeability and the permeability of the protolith rocks

([7]). In this way the permeability contrasts between damage zone and fault core (k_d/k_c) are maintained constants depending on the type of protolith that the fault core intersects. In particular in Model$_3$ the permeability of the damage zone is one order of magnitude higher than the permeability of the protolith ($k_d/k_p = 10^1$; Table 1,2 and 3) whereas the fault core permeability is four orders of magnitude lower than the permeability of the damage zone ($k_d/k_c = 10^4$; Table 2,3). In Model$_4$ the permeability of the damage zone is still one order of magnitude higher than the permeability of the protolith ($k_d/k_p = 10^1$; Table 1, 2, and 3) but the fault core permeability is in this case five orders of magnitude lower than the permeability of the damage zone ($k_d/k_c = 10^5$; Table 2, 3). In Model$_5$ the permeability of the damage zone is two orders of magnitude higher than the permeability of the protolith ($k_d/k_p = 10^2$; Table 1, 2, and 3) and the fault core permeability is five orders of magnitude lower than the permeability of the damage zone ($k_d/k_c = 10^5$; Table 2, 3). In the last model (Model$_6$) the permeability of the damage zone is two orders of magnitude higher than the permeability of the protolith ($k_d/k_p = 10^2$; Table 1, 2, and 3) and the fault core permeability is in this case six orders of magnitude lower than the permeability of the damage zone ($k_d/k_c = 10^6$; Table 2, 3).

3 Results

Figure 5 shows the variation of the effective normal stress ($\Delta\sigma'_n$) and shear stress ($\Delta\tau$) calculated on the faults F1, F2, F3 and F4 for different models. The points where $\Delta\sigma'_n$ and $\Delta\tau$ are calculated have the same y and z coordinates as the injection point and hence are located in the storage aquifer (the location is shown in Figure 2c). $\Delta\sigma'_n$ and $\Delta\tau$ are obtained as the difference of the values σ'_n and τ calculated in the injection step minus the values of σ'_n and τ calculated at the initial geostatic step (squares along the colour lines in Figure 5).

For all the faults in Figure 5 we observe that $\Delta\sigma'_n$ always decreases as a consequence of an increase in the pore pressure. The only difference is that the magnitude of this drop depends mainly on the contrast of permeability between damage zone and protolith rock. In fact, by considering fault F1 (Figure 5a) we observe that the evolution of $\Delta\sigma'_n$ is very similar for the Model$_1$, Model$_2$, Model$_3$ and Model$_4$. At the end of the simulation the effective normal stress decreases of almost 3.5 MPa. These models present the same ratio $k_d/k_p = 10^1$. On the contrary, for Model$_4$ and Model$_5$ $\Delta\sigma'_n$ is close to 1.5 MPa. In these models the contrast of permeability k_d/k_p is equal to 10^2. If on one hand the contrast

Parameters	Storage aquifer	Caprock	Upper aquifer	Basal aquifer	Fault damage zone	Fault core
Youngs modulus E (GPa)	10	10	10	10	10	10
Poissons ratio ν	0.25	0.25	0.25	0.25	0.25	0.25
Rock density ρ_s (Kg/m^3)	2260	2260	2260	2260	2260	2260
Porosity ϕ ϕ	0.1	0.01	0.1	0.01	Equal to the corresponding hydrological layer	Equal to the corresponding hydrological layer
Permeability $\boldsymbol{k}$ (m^2)	10^{-13}	10^{-19}	10^{-14}	10^{-16}	Variable (Table 2, 3)	Variable (Table 2, 3)
Saturation s	1	1	1	1	1	1

Table 1: Material properties used to simulate water injection in a faulted storage aquifer-caprock system. These properties are maintained constant in all models. The permeability in the fault zone is the only parameter that varies (see Table 2 and Table 3 for detail).
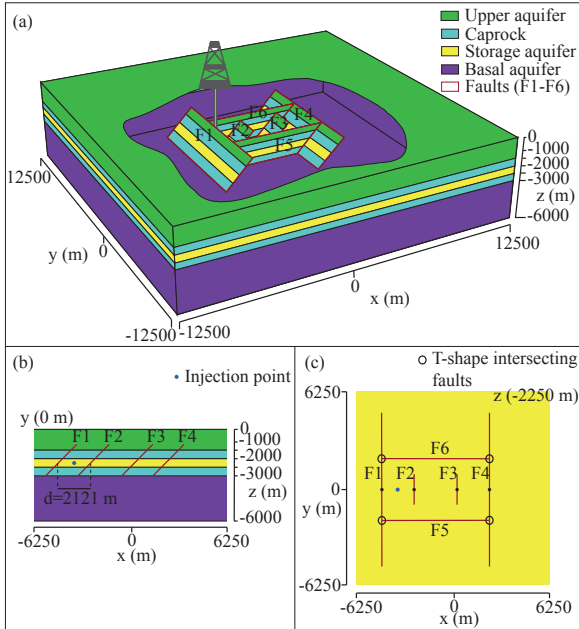
Fig. 3: (a) Model geometry for the coupled simulation of water injection and fault slip. (b) Cross-sections along the xz-plane and (c) xy-plane crossing the water injection point. Note that the F1 and F4 faults form T-shape intersections with the F6 and F5 faults. The hydro-mechanical properties are described in table 1. The black points on the F1, F2, F3 and F4 faults represent the location where $\Delta\sigma'_n$, $\Delta\tau$ and slip are calculated in Figure 5 and Figure 7.

of permeability k_d/k_p determine the evolution of $\Delta\sigma'_n$ on the fault plane, on the other hand the contrast of permeability k_d/k_c affects the evolution of $\Delta\tau$.
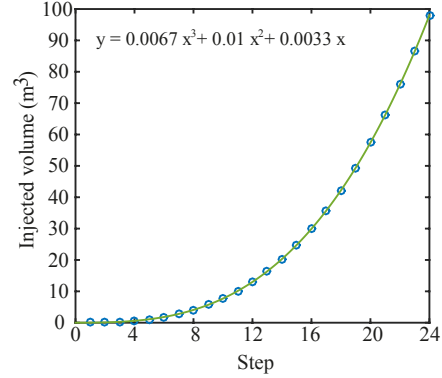
Fig. 4: Volume of water injected for every simulation step. The total volume of water injected at the end of the numerical simulation is 98 m^3.

Damage zone	Storage aquifer	Caprock	Upper aquifer	Basal aquifer
Model$_1$	10^{-12}	10^{-18}	10^{-13}	10^{-15}
Model$_2$	10^{-12}	10^{-18}	10^{-13}	10^{-15}
Model$_3$	10^{-12}	10^{-18}	10^{-13}	10^{-15}
Model$_4$	10^{-12}	10^{-18}	10^{-13}	10^{-15}
Model$_5$	10^{-11}	10^{-17}	10^{-12}	10^{-14}
Model$_6$	10^{-11}	10^{-17}	10^{-12}	10^{-14}

Table 2: Variation of permeability across the damage zone for different models considered. Note that the permeability varies depending on the minimal distance from the faults (see text and Figure 1 for details).

Let us consider again the trends of $\Delta\sigma'_n$ and $\Delta\tau$ on the fault F1 (Figure 5a). Model$_1$ and Model$_2$ have the same contrast of permeability between damage zone and protolith rock ($k_d/k_p = 10^1$) but different contrasts

Fault core	Storage aquifer	Caprock	Upper aquifer	Basal aquifer
Model$_1$	10^{-22}	10^{-22}	10^{-22}	10^{-22}
Model$_2$	10^{-16}	10^{-16}	10^{-16}	10^{-16}
Model$_3$	10^{-16}	10^{-22}	10^{-17}	10^{-19}
Model$_4$	10^{-17}	10^{-23}	10^{-18}	10^{-20}
Model$_5$	10^{-16}	10^{-22}	10^{-17}	10^{-19}
Model$_6$	10^{-17}	10^{-23}	10^{-18}	10^{-20}

Table 3: Variation of permeability across the fault core for different models considered. Note that the permeability varies depending on the minimal distance from the faults (see text and Figure 1 for details).
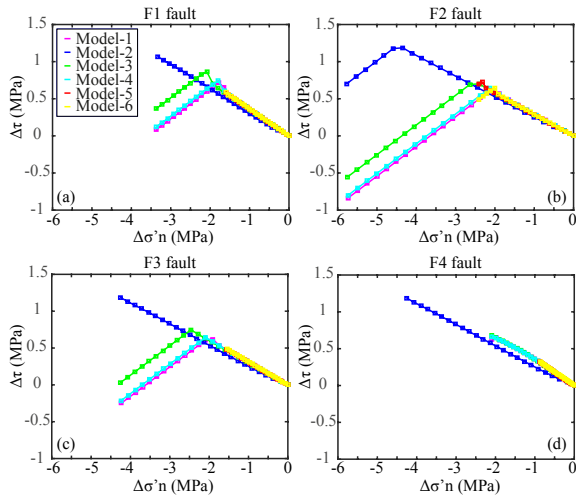
Fig. 5: Evolution of the effective normal stress $\Delta\sigma'_n$ and shear stress $\Delta\tau$ variations along F1, F2, F3 and F4 faults for different models. Note the drop of shear stress when the faults reach the failure.

Fig. 6: Variation of pore pressure after 98 m^3 of injected water.

of permeability between damage zone and fault core. Note that this contrast k_d/k_c is not constant along the dip of the faults, because in these models we assume uniform permeability values of the fault core in the direction of the fault dip. For this reason the contrast k_d/k_c varies depending on the type of protolith that the fault intersects (Table 2, 3). For example the contrast of permeability k_d/k_c inside the storage aquifer is equal to 10^1 and 10^4 for the Model$_1$ and Model$_2$ respectively, while the contrast of permeability k_d/k_c inside the caprock is equal to 10^4 and 10^2 for the Model$_1$ and Model$_2$ respectively. Hence in the Model 1, water is well compartmentalized both in the normal direction and along the dip direction respect to the fault plane. For this reason the shear stress increases more in Model$_1$ than in Model$_2$ where the fault F1 never reaches the failure (Figure 5a). Model$_3$ and Model$_4$ have the same contrast of permeability between damage zone and pro-

tolith rock ($k_d/k_p = 10^1$) but different contrasts of permeability between damage zone and fault core. In these cases the contrast k_d/k_c is constant along the dip of the faults. Indeed the contrast of permeability k_d/k_c inside the storage aquifer and caprock is always equal to 10^4 and 10^5 for Model$_3$ and Model$_4$ respectively. In Model$_4$, the fault F1 reaches failure before Model$_3$ with a trend very similar to that obtained for the Model$_1$ (Figure 5a). The evolution of $\Delta\sigma'_n$ and $\Delta\tau$ is very similar for the other faults (Figure 5b-d) but with different times of failure depending on the distance between the injection point and the faults. F2 fault is the only one that reaches failure in all the models. The effects of the contrast of permeability between the fault core and damage zone on $\Delta\tau$ are well visible also by analysing the trend of Model$_5$ and Model$_6$ on the fault F2 (Figure 5b). In these models the ratio k_d/k_p is the same (10^2) but the ratio k_d/k_c is equal to 10^5 and 10^6 for Model$_5$ and Model$_6$ respectively. Also in these cases, by considering the same $\Delta\sigma'_n$, the fault F2 reaches the failure earlier in Model$_6$ than Model$_5$. Note that $\Delta\tau$ increases

until the strength of the fault is overcome and then it decreases continuously following the static friction law.
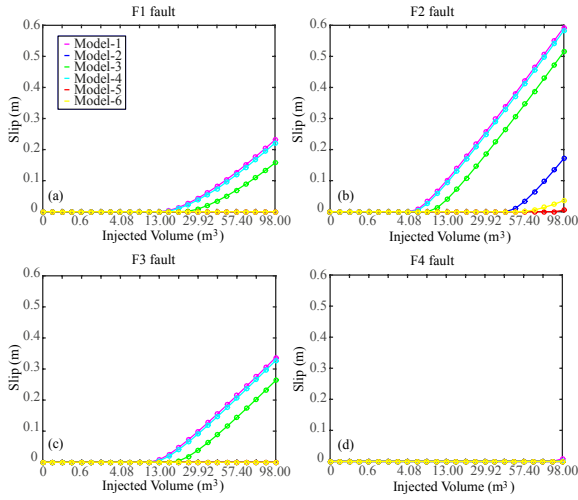
Fig. 7: Slip evolution along the F1, F2, F3 and F4 faults for different models.

Figure 6 shows the variation of the pore pressure after 98 m³ of injected water. It is well visible that the contrast of permeability between the damage zone and protolith rock has a larger effect on the pore pressure distribution than the contrast of permeability between the damage zone and fault core. In fact in $Model_5$ and $Model_6$ (Figure 6e and 6f) where $k_d/k_c = 10^2$, the variation of pore pressure on the injection point is less than the other models where $k_d/k_c = 10^1$. This effect is partially due to the proximity of the injection point to the damage zone and partially to the larger thickness of the damage zone respect to the fault core.

Figure 7 shows the slip evolution along the F1, F2, F3 and F4 faults for different models. Slip is calculated on points located in the central part of each fault inside the storage aquifer (Figure 3c). In this figure we observe the steps where the faults starts to slip. Slip on one fault occurs before than others in the models where the fluids are well compartmentalized by the fault core, both in the normal and dip direction to the fault plane ($Model_1$, and $Model_4$). In other models, no slip occurs because large values of permeability of the damage zone allow the fluids to move freely into the storage aquifer, without generating high values of pore pressure (e.g. $Model_5$ and $Model_6$ on fault F1 and F2). The distribution of the slip is very similar in the $Model_1$ and $Model_4$ (Figure 8a and 8d). Note that the slip propagates outside the storage aquifer into the caprock and in same models also into the upper aquifer (Figure 8a, 8c and 8d). In fact,
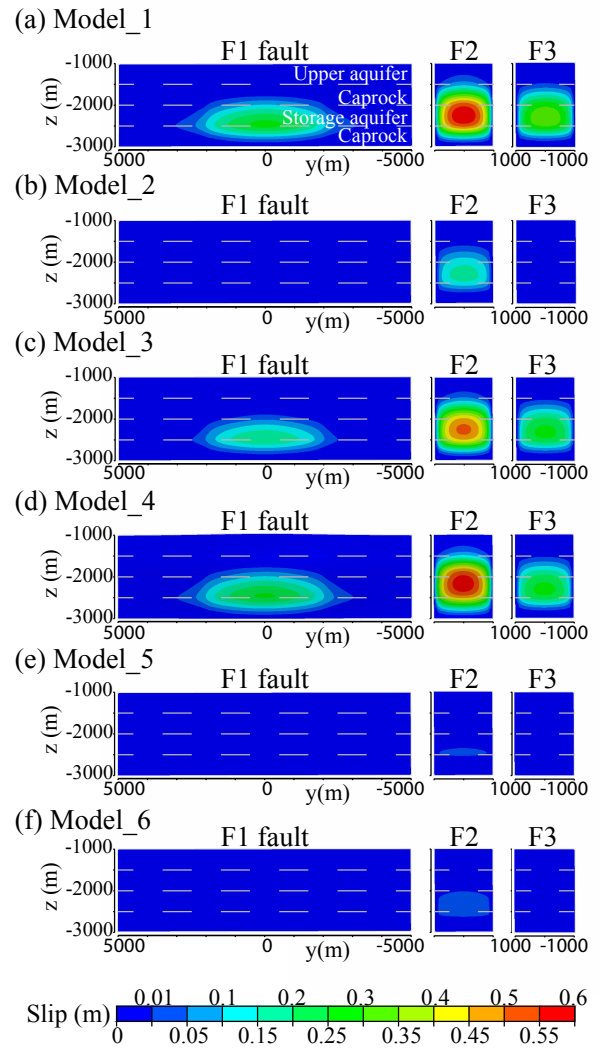
Fig. 8: Cumulative slip along the F1, F2 and F3 faults for different models.

fault F2 fails before the others and for this reason accumulates more slip during the different injection steps. In addition fault F2 is narrow along the strike direction and hence the slip propagates mainly along the dip. Finally, Figure 9 shows the vertical displacement along the xz plane cutting the injection point. Also in this case we shows the results for the last injection step and hence the vertical displacement includes the contributions both from the injected water and from the fault slip. The thrust-fault regime governs the kinematic of the faults, with the hanging wall moving up with respect to the footwall. This is also visible on the fault F2 (Figure 9a-9d).
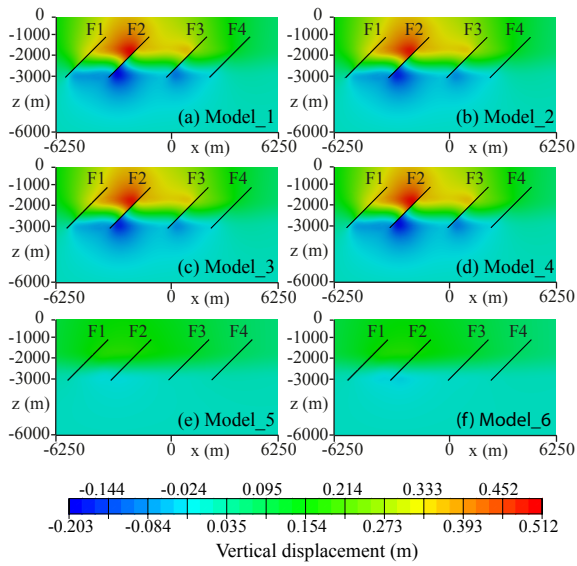
Fig. 9: Final vertical displacement along a xz plane across the water injection point.

4 Discussion

Before interpreting the results, it is necessary to discuss briefly the limitations of the models. First, in all these models, a quasi-static approximation is considered to simulate the evolution of the slip along the fault. Hence no transient effects are considered. In fact, during the coseismic phase, the inertial term could be significant due to the propagation of seismic waves and hence affect the slip along the fault plane. In addition, a static friction constitutive model is used to describe the slip evolution along the fault planes. This friction model does not permit the drop between a static to a dynamic friction value (e.g. slip weakening friction [22]) typical of earthquakes, neither the evolution of the friction during the interseismic phase of the seismic cycle (rate-and state friction [14]). For this reason the earthquake magnitude calculations will be discussed with caution. A second limitation concerns the elastic properties that, in this study, are assumed constants. Different measurements on fault rock sample demonstrate that the Young modulus and Poisson ratio can change significantly and hence can affect the stress build-up along the fault planes [19,15]. This choice was made consciously in order to estimate only the contribution of the permeability variation across the fault zone. A final limitation is related to the time-evolution of the permeability across the fault zone. Indeed, different geological [37,11] and seismological observations [20] show that the permeability can vary during different phases of the seismic cycle. Well-known permeability-porosity

relationships are considered in the literature [36,42,12] and used in coupled fluid flow and geomechanical models (e.g. [9]). However this work is more devoted to the understanding of the static aspects of triggered seismicity (e.g. timing of fault reactivation) than to the dynamic processes involved in this phenomena. However, in spite of these limitations, a number of interesting statements can be inferred on the basis of the present results. The variation of permeability along the normal direction of the fault plane affects the failure time of the faults that in these synthetic tests is expressed in terms of different steps of water injected. In particular, considering the same contrast of permeability between damage zone and protolith inside the storage aquifer, it is necessary to inject more water in order to reach the failure in the case where the contrast of permeability between damage zone and fault core is lower (e.g. $Model_3$, Figure 7). Otherwise considering the same contrast of permeability between damage zone and fault core (e.g. $Model_4$ and $Model_5$), also inside the storage aquifer, it is necessary to inject more water in order to reach the failure in the case where the contrast of permeability between damage zone and protolith is largest (e.g. $Model_5$). This is because, depending on its absolute permeability, the fault core acts as a barrier to the fluid flow. More precisely, the smaller the absolute permeability is, the larger the increase of the pore pressure across the fault, which leads to a large decreasing of the effective normal stress for the same volume of water injected (Figure 5). However also the variation of permeability inside the fault core layer and along the tangential direction of the fault plane has a strong effect on the timing of the triggered earthquakes. Indeed by considering inside the storage aquifer the same contrast of permeability between damage zone and protolith and damage zone and fault core ($Model_2$ and $Model_3$), it is necessary to inject more water in order to reach the failure in the case where the permeability does not change in the fault core along the tangential direction of the fault plane ($Model_2$; Figure 7b). This behavior is due to a different hydrological response of the fault zones. In fact in $Model_3$ the fluids are well compartmentalized inside the reservoir due to the increase of the fault core permeability versus the caprocks layers. This leads to the increase of pore pressure relatively to the $Model_2$ (Figure 5), where the fault core permeability is maintained constant in the fault dip direction. Of course, this effect is more evident if the absolute permeability of the fault core is low. In the other cases, when the permeability inside the fault core is large and homogeneous, the effects of the variation of permeability along the tangential direction of the fault plane are negligible because the fault core acts like a barrier to the fluid flow.

Few data of fault zone hydrological properties are available in literature and are often based on the analysis of exhumed fault zones [7,16,47,15]. However, the present models demonstrate that the spatial variation of the permeability inside the fault zone (including fault core and damage zone) affects the timing of the triggered earthquakes. This could explain the variability of cases where fluids injection does not generate relevant seismicity (e.g. [18]). The different contrast of permeability affects the magnitude of the triggered earthquakes (Table 4). We consider the magnitude of the final slip $\|\boldsymbol{d}\|$ at the last injection step to calculate the earthquake magnitude:

$$M_w = \frac{2}{3} \log_{10} M_0 - 6.0 \qquad (11)$$

where $M_0 = \int_\Gamma G\|\boldsymbol{d}\| d\Gamma$ is the seismic moment and G is the shear modulus ([21]). We remark that our simulations are quasi-static. For this reason earthquake refers to the seismic event producing an equivalent amount of slip ([23]). In table 4 it is evident that for the same volume of injected fluid and considering the same fault, an earthquake with larger magnitude is expected when the faults act as a barrier (very low permeability) to the fluid flow both along the normal and tangential direction with respect to the fault plane (Model$_1$ and Model$_4$). This aspect is fundamental to estimate the maximum earthquake magnitude expected during fluid injection. On the basis of the analysis of numerous case histories of earthquake sequences induced by fluid injection, [28] has demonstrated that the maximum earthquake magnitude is correlated to the total volume of fluid injected times the modulus of rigidity. If, on the one hand, it could be considered a fast method to estimate the maximum magnitude of the induced earthquake, on the other hand our results demonstrate that the initial state of stress along the faults as well as the hydrological properties of the fault zone could be decisive in estimating of the effective magnitude of the triggered earthquakes. For this reason, we suggest that these variables should be included in new relationships devoted to estimate the effective magnitude of the induced and triggered earthquakes.

5 Conclusions

In this work, we studied the effects of the spatial variation of the fault zone permeability on the timing and magnitude of triggered earthquakes by water injection in synthetic faulted storage aquifers. Considering the variation of permeability along the normal direction of the fault plane, large contrasts of permeability between damage zone and protolith rocks can increase the recurrence time of the triggered earthquake. Conversely, large contrasts of permeability between damage zone and fault core can reduce the time of the triggered earthquake. However the effects of the permeability contrast between damage zone and fault core are depending also on the absolute permeability of the fault core. The lower the absolute permeability of the fault core is, the lower the dependency of the timing of the triggered earthquake on the contrast of permeability across the damage zone and fault core. This is because the fault core acts as a localized barrier. In addition, another important conclusion is that the variation of fault core permeability along the tangential direction of the fault plane can also affect significantly the pore pressure distribution along the fault plane. This effect is evident when the permeability along the fault core varies from larger values for the part of fault core cutting the storage aquifer to lower values for the parts of fault core cutting the caprocks. In this way the fluids are well compartmentalized, increasing the pore pressure along the fault surface. We conclude that the complex architecture of the fault zone should be included in fluid-flow and geomechanical simulations devoted to the evaluation of the stability of the faults during fluid injection. This is a fundamental step towards the understanding of the timing and magnitude of induced and triggered earthquakes.

References

1. Aagaard, B.T., Knepley, M.G., Williams, C.A.: A domain decomposition approach to implementing fault slip in finite-element models of quasi-static and dynamic crustal deformation. Journal of Geophysical Research: Solid Earth **118**(6), 3059–3079 (2013). DOI 10.1002/jgrb.50217
2. ABAQUS: Theory Manual, Version 6.13. Providence, Rhode Island (2013)
3. Bear, J.: Dynamics of Fluids in Porous Media. John Wiley, New York, N. Y (1972)
4. Brown, K., Kopf, A., Underwood, M., Weinberger, J.: Compositional and fluid pressure controls on the state of stress on the Nankai subduction thrust: A weak plate boundary. Earth and Planetary Science Letters **214**(3-4), 589–603 (2003). DOI 10.1016/S0012-821X(03)00388-1
5. Bruhn, R.L., Parry, W.T., Yonkee, W.A., Thompson, T.: Fracturing and hydrothermal alteration in normal fault zones. pure and applied geophysics **142**(3), 609–644 (1994). DOI 10.1007/BF00876057
6. Byerlee, J.: Friction of rocks. pure and applied geophysics **116**(4), 615–626 (1978). DOI 10.1007/BF00876528

M_w	Model$_1$	Model$_2$	Model$_3$	Model$_4$	Model$_5$	Model$_6$
F1	4.33	2.41	4.17	4.26	-	2.36
F2	4.44	4.00	4.39	4.41	3.01	3.48
F3	4.20	2.46	4.16	4.21	0.47	1.62
F4	3.13	-	-	1.64	-	-

Table 4: Earthquake magnitude (M_w) calculations on well-orientend dipping faults for different models

7. Caine, J.S., Evans, J.P., Forster, C.B.: Fault zone architecture and permeability structure. Geology **24**(11), 1025–1028 (1996). DOI 10.1130/0091-7613(1996)024¡1025:FZAAPS¿2.3.CO;2

8. Cappa, F., Rutqvist, J.: Impact of CO 2 geological sequestration on the nucleation of earthquakes. Geophysical Research Letters **38**(17), n/a–n/a (2011). DOI 10.1029/2011GL048487

9. Cappa, F., Rutqvist, J.: Modeling of coupled deformation and permeability evolution during fault reactivation induced by deep underground injection of CO2. International Journal of Greenhouse Gas Control **5**(2), 336–346 (2011). DOI 10.1016/j.ijggc.2010.08.005

10. Catalli, F., Meier, M.A., Wiemer, S.: The role of Coulomb stress changes for injection-induced seismicity: The Basel enhanced geothermal system. Geophysical Research Letters **40**(1), 72–77 (2013). DOI 10.1029/2012GL054147

11. Chester, F.M., Evans, J.P., Biegel, R.L.: Internal structure and weakening mechanisms of the San Andreas Fault. Journal of Geophysical Research: Solid Earth **98**(B1), 771–786 (1993). DOI 10.1029/92JB01866

12. Chin, L.Y., Raghavan, R., Thomas, L.K.: Fully Coupled Geomechanics and Fluid-Flow Analysis of Wells With Stress-Dependent Permeability. SPE journal (2000). DOI 10.2118/58968-PA

13. Collettini, C., Niemeijer, A., Viti, C., Marone, C.: Fault zone fabric and fault weakness. Nature **462**(7275), 907–910 (2009)

14. Dieterich, J.H.: Modeling of rock friction: 1. Experimental results and constitutive equations. Journal of Geophysical Research **84**(B5), 2161 (1979). DOI 10.1029/JB084iB05p02161

15. Faulkner, D.R., Mitchell, T.M., Healy, D., Heap, M.J.: Slip on 'weak' faults by the rotation of regional stress in the fracture damage zone. Nature **444**(7121), 922–925 (2006)

16. Faulkner, D.R., Rutter, E.H.: Can the maintenance of overpressured fluids in large strike-slip fault zones explain their apparent weakness? Geology **29**(6), 503–506 (2001). DOI 10.1130/0091-7613(2001)029¡0503:CTMOOF¿2.0.CO;2

17. Forster, C.B., Evans, J.P.: Hydrogeology of thrust faults and crystalline thrust sheets: Results of combined field and modeling studies. Geophysical Research Letters **18**(5), 979–982 (1991). DOI 10.1029/91GL00950

18. Frohlich, C., Walter, J.I., Gale, J.F.W.: Analysis of Transportable Array (USArray) Data Shows Earthquakes Are Scarce near Injection Wells in the Williston Basin, 2008?2011. Seismological Research Letters **86**(2A), 492–499 (2015). DOI 10.1785/0220140180

19. Gudmundsson, A.: Effects of Young's modulus on fault displacement. Comptes Rendus Geoscience **336**(1), 85–92 (2004). DOI 10.1016/j.crte.2003.09.018

20. Guglielmi, Y., Cappa, F., Avouac, J.P., Henry, P., Elsworth, D.: Seismicity triggered by fluid injection?induced aseismic slip. Science **348**(6240), 1224–1226 (2015)

21. Hanks, T.C., Kanamori, H.: A moment magnitude scale. Journal of Geophysical Research **84**(B5), 2348 (1979). DOI 10.1029/JB084iB05p02348

22. Ida, Y.: The maximum acceleration of seismic ground motion. Bulletin of the Seismological Society of America **63**(3), 959–968 (1973)

23. Jha, B., Juanes, R.: Coupled multiphase flow and poromechanics: A computational model of pore pressure effects on fault slip and earthquake triggering. Water Resources Research **50**(5), 3776–3808 (2014). DOI 10.1002/2013WR015175

24. Keranen, K.M., Savage, H.M., Abers, G.A., Cochran, E.S.: Potentially induced earthquakes in Oklahoma, USA: Links between wastewater injection and the 2011 Mw 5.7 earthquake sequence. Geology (2013). DOI 10.1130/G34045.1

25. Kim, J., Tchelepi, H., Juanes, R.: Stability and convergence of sequential methods for coupled flow and geomechanics: Fixed-stress and fixed-strain splits. Computer Methods in Applied Mechanics and Engineering **200**(13-16), 1591–1606 (2011). DOI 10.1016/j.cma.2010.12.022

26. Lockner, D.A., Morrow, C., Moore, D., Hickman, S.: Low strength of deep San Andreas fault gouge from SAFOD core. Nature **472**(7341), 82–85 (2011)

27. Lockner, D.A., Tanaka, H., Ito, H., Ikeda, R., Omura, K., Naka, H.: Geometry of the Nojima Fault at Nojima-Hirabayashi, Japan – I. A Simple Damage Structure Inferred from Borehole Core Permeability. Pure and Applied Geophysics **166**(10), 1649–1667 (2009). DOI 10.1007/s00024-009-0515-0

28. McGarr, A.: Maximum magnitude earthquakes induced by fluid injection. Journal of Geophysical Research: Solid Earth **119**(2), 1008–1019 (2014). DOI 10.1002/2013JB010597

29. Mitchell, T., Faulkner, D.: Towards quantifying the matrix permeability of fault damage zones in low porosity rocks. Earth and Planetary Science Letters **339-340**, 24–31 (2012). DOI 10.1016/j.epsl.2012.05.014

30. Moeck, I., Kwiatek, G., Zimmermann, G.: Slip tendency analysis, fault reactivation potential and induced seismicity in a deep geothermal reservoir. Journal of Structural Geology **31**(10), 1174–1182 (2009). DOI 10.1016/j.jsg.2009.06.012

31. Oda, M., Hatsuyama, Y., Ohnishi, Y.: Numerical experiments on permeability tensor and its application to jointed granite at Stripa Mine, Sweden. Journal of Geophysical Research **92**(B8), 8037 (1987). DOI 10.1029/JB092iB08p08037

32. Rubinstein, J.L., Ellsworth, W.L., McGarr, A.F., Benz, H.M.: The 2001-present induced earthquake sequence in the Raton Basin of northern New Mexico and southern Colorado. Bulletin of the Seismological Society of America **104**(5), 2162–2181 (2014). DOI 10.1785/0120140009

33. Rutqvist, J., Birkholzer, J., Tsang, C.F.: Coupled reservoir?geomechanical analysis of the potential for tensile and shear failure associated with CO2 injection in multi-layered reservoir?caprock systems. International Journal

of Rock Mechanics and Mining Sciences **45**(2), 132–143 (2008). DOI 10.1016/j.ijrmms.2007.04.006

34. Rutqvist, J., Wu, Y.S., Tsang, C.F., Bodvarsson, G.: A modeling approach for analysis of coupled multiphase fluid flow, heat transfer, and deformation in fractured porous rock. International Journal of Rock Mechanics and Mining Sciences **39**(4), 429–442 (2002). DOI 10.1016/S1365-1609(02)00022-9

35. Saffer, D.M., Marone, C.: Comparison of smectite- and illite-rich gouge frictional properties: application to the updip limit of the seismogenic zone along subduction megathrusts. Earth and Planetary Science Letters **215**(1-2), 219–235 (2003). DOI 10.1016/S0012-821X(03)00424-2

36. Scheidegger, A.: The Physics of Flow Through Porous Media. University of Toronto Press, Toronto (1974)

37. Sibson, R.H.: Fluid Flow Accompanying Faulting: Field Evidence and Models. In: Earthquake Prediction, pp. 593–603. American Geophysical Union (1981). DOI 10.1029/ME004p0593

38. Sibson, R.H.: Thickness of the Seismic Slip Zone. Bulletin of the Seismological Society of America **93**(3), 1169–1178 (2003). DOI 10.1785/0120020061

39. Streit, J.E., Hillis, R.R.: Estimating fault stability and sustainable fluid pressures for underground storage of CO2 in porous rock. Energy **29**(9-10), 1445–1456 (2004). DOI 10.1016/j.energy.2004.03.078

40. Sumy, D.F., Cochran, E.S., Keranen, K.M., Wei, M., Abers, G.A.: Observations of static Coulomb stress triggering of the November 2011 M 5.7 Oklahoma earthquake sequence. Journal of Geophysical Research: Solid Earth **119**(3), 1904–1923 (2014). DOI 10.1002/2013JB010612

41. Talwani, P., Acree, S.: Pore pressure diffusion and the mechanism of reservoir-induced seismicity. pure and applied geophysics **122**(6), 947–965 (1984). DOI 10.1007/BF00876395

42. TD, V.G.R.: Fundamentals of Fractured Reservoir Engineering. Elsevier, Amsterdam (1982)

43. Townend, J., Zoback, M.D.: How faulting keeps the crust strong. Geology **28**(5), 399–402 (2000). DOI 10.1130/0091-7613(2000)28¡399:HFKTCS¿2.0.CO;2

44. Troiano, A., Di Giuseppe, M.G., Troise, C., Tramelli, A., De Natale, G.: A Coulomb stress model for induced seismicity distribution due to fluid injection and withdrawal in deep boreholes. Geophysical Journal International (2013). DOI 10.1093/gji/ggt229

45. Uehara, S.i., Shimamoto, T.: Gas permeability evolution of cataclasite and fault gouge in triaxial compression and implications for changes in fault-zone permeability structure through the earthquake cycle. Tectonophysics **378**(3?4), 183–195 (2004). DOI http://dx.doi.org/10.1016/j.tecto.2003.09.007

46. Weingarten, M., Ge, S., Godt, J.W., Bekins, B.a., Rubinstein, J.L.: High-rate injection is associated with the increase in U.S. mid-continent seismicity. Science **348**(6241), 1336–1340 (2015). DOI 10.1126/science.aab1345

47. Wibberley, C.A.J., Shimamoto, T.: Internal structure and permeability of major strike-slip fault zones: the Median Tectonic Line in Mie Prefecture, Southwest Japan. Journal of Structural Geology **25**(1), 59–78 (2003). DOI http://dx.doi.org/10.1016/S0191-8141(02)00014-7

48. Wiprut, D., Zoback, M.D.: Fault reactivation and fluid flow along a previously dormant normal fault in the northern North Sea. Geology **28**(7), 595–598 (2000). DOI 10.1130/0091-7613(2000)28¡595:FRAFFA¿2.0.CO;2

MOX Technical Reports, last issues

Dipartimento di Matematica
Politecnico di Milano, Via Bonardi 9 - 20133 Milano (Italy)

60/2017   Bonaldi, F.; Di Pietro, D. A.; Geymonat, G.; Krasucki, F.
A Hybrid High-Order method for Kirchhoff-Love plate bending problems

59/2017   Grujic, O.; Menafoglio, A.; Guang, Y.; Caers, J.
Cokriging for multivariate Hilbert space valued random fields. Application to multifidelity computer code emulation

58/2017   Landajuela, M.; Vergara, C.; Gerbi, A.; Dede', L.; Formaggia, L.; Quarteroni, A.
Numerical approximation of the electromechanical coupling in the left ventricle with inclusion of the Purkinje network

56/2017   Alberti, G. S.; Santacesaria, M.
Infinite dimensional compressed sensing from anisotropic measurements

57/2017   Ballarin, F.; D'Amario, A.; Perotto, S.; Rozza, G.
A POD-Selective Inverse Distance Weighting method for fast parametrized shape morphing

53/2017   Bertagna, L.; Deparis, S.;Formaggia, L.; Forti, D.; Veneziani A.
The LifeV library: engineering mathematics beyond the proof of concept

55/2017   Agosti, A.; Cattaneo, C.; Giverso, C.; Ambrosi, D.; Ciarletta, P.
A computational platform for the personalized clinical treatment of glioblastoma multiforme

54/2017   Dede', L; Quarteroni, A.
Isogeometric Analysis of a Phase Field Model for Darcy Flows with Discontinuous Data

52/2017   Beretta, E.; Ratti, L.; Verani, M.
A phase-field approach for the interface reconstruction in a nonlinear elliptic problem arising from cardiac electrophysiology

51/2017   Gerbi, A.; Dede', L.; Quarteroni, A.
A monolithic algorithm for the simulation of cardiac electromechanics in the human left ventricle